Acta Astronautica 226 (2025) 521–530

Contents lists available at ScienceDirect

Acta Astronautica

journal homepage: www.elsevier.com/locate/actaastro

Research paper

Effect of input power on plasma expansion and ion acceleration in a radio-frequency plasma thruster

Antonella Caldarelli [a,c,*], Raoul Andriulli [a], Fabrizio Ponti [a], John Cater [b], Nicholas Rattenbury [c]

[a] Department of Industrial Engineering, University of Bologna, Via Fontanelle 40, Forlì, Italy
[b] Department of Mechanical Engineering, University of Canterbury, Christchurch, New Zealand
[c] Department of Physics, The University of Auckland, 38 Princes Street, Auckland, New Zealand

ARTICLE INFO

Keywords:
Plasma thruster
Magnetic nozzle
Ion beam
RF plasmas

ABSTRACT

Exploring the physics of low pressure plasmas expanding in a diverging magnetic nozzle, and the resulting acceleration mechanisms, plays an important role in the development of a new-type of electrode-less plasma propulsion systems. This study discusses the effects of input power on plasma expansion and ion beam acceleration in a magnetic nozzle electrode-less plasma thruster. The experiments were conducted in a radio-frequency magnetic nozzle plasma device at The University of Auckland with four different power configurations P_{RF}. Different plasma diagnostics were used to measure the characteristics of the plasma plume. A planar Langmuir probe was used to measure the floating potential and ion saturation current both in the plasma source and in the expansion chamber. The potential drop in the plasma source was obtained with an emissive probe. A retarding field energy analyser was employed to evaluate the local plasma and ion beam potentials, the ion energy distribution functions, and to estimate the ion beam speed in the expansion region. Measurements showed that, as expected, increasing the power input resulted in a higher plasma and supersonic ion density, while the ion beam speed did not increase further for $P_{RF} > 100$ W. Interestingly, and contrary to the idealised physical model, the ion sonic transition did not occur at the magnetic nozzle throat, but instead close to the geometrical expansion point, i.e. near the interface between the source tube and the expansion chamber. This feature would result in a lower performance of the thruster given the reduced expansion ratio. An E-H mode change is also observed to occur in the device with increasing radio-frequency power that would help explain the different plasma characteristics observed at the 200 W transition point.

1. Introduction

A new attraction for low-pressure plasmas expanding in a magnetic field has been found in the electric propulsion industry as space travel has become more accessible to private and research purposes, and with the desire to pursue further interplanetary, deep-space missions. Furthermore, the aerospace industry has recently seen a boom in the manufacturing of small and nano-scale satellites for space communications, environmental and weather monitoring, and scientific research. The miniaturisation of spacecraft means that they are cheaper to build, cheaper to launch and provide greater flexibility when designing a space mission. However, their size poses restrictions in terms of mass, volume and power budget. A propulsion system capable of providing very high exhaust velocities is desirable as the propellant mass required to perform a certain mission is significantly reduced. These exhaust velocities cannot be obtained by conventional chemical rockets. As the required exhaust velocities can currently be achieved solely by electric propulsion, they are a more attractive option for small-satellites and interplanetary missions requiring a high propellant efficiency [1]. A successful example of the use of electric propulsion systems for deep-space travel can be found in the European Space Agency's *BepiColombo* spacecraft, which was equipped with four T6 gridded ion thrusters [2].

Magnetic nozzle (MN) radio-frequency (RF) plasma thrusters, sometimes referred to as Helicon Plasma Thrusters, are a type of electric propulsion system that employs radio-frequency excitation to generate the plasma and a convergent-divergent magnetic field (i.e., a magnetic nozzle) to enhance plasma acceleration and confinement, and to convert the electron internal energy into the directed kinetic energy of the ions [3–7]. This new technology has received a lot of interest in the electric propulsion community in the last two decades, as its numerous benefits could make it a competitive choice for future low-thrust space missions. When compared to gridded ion engines and Hall Effect thrusters, the lack of electrodes and neutralisers of the RF plasma thruster's design, together with the advantage of a magnetic

* Corresponding author at: Department of Industrial Engineering, University of Bologna, Via Fontanelle 40, Forlì, Italy.
E-mail address: antonella.caldarelli@unibo.it (A. Caldarelli).

https://doi.org/10.1016/j.actaastro.2024.10.055
Received 23 August 2024; Received in revised form 6 October 2024; Accepted 22 October 2024
Available online 1 November 2024

List of Abbreviations

CCP	Capacitively Coupled Plasma
EP	Emissive Probe
ICP	Inductively Coupled Plasma
IEDF	Ion Energy Distribution Function
LP	Langmuir Probe
MN	Magnetic Nozzle
RF	Radio-Frequency
RFEA	Retarding Field Energy Analyser

nozzle in improving plasma confinement, could increase the lifetime of the propulsion system. Additionally, the concept of magnetic thrust vectoring for radio-frequency plasma thrusters, which relies on a steerable magnetic nozzle to control the direction of the plasma plume, has been studied [8–13]. Thus, the capability to tune the magnetic field configuration could enable full modulation of the in-flight thrust profile of the spacecraft.

For propulsion applications, it is important to fully understand the expansion of a supersonic ion beam in a magnetic nozzle as it is one of the main thrust generation mechanisms in electrode-less radio-frequency plasma thrusters. With the first measurement of the spontaneous generation of an accelerated, supersonic ion beam via a current-free double-layer in a helicon source [14] and the subsequent development of the Helicon Double-Layer Thruster [3], efforts have been made to further develop the technology [4–7,15–20]. When compared to current state-of-the-art electric propulsion systems, the performance of these thrusters remains too low for them to be a competitive alternative to existing thrusters. Indeed, the highest thruster efficiency obtained so far in an experimental campaign was reported to be 30% [21], compared to a 65%–80% propulsive efficiency of current electrostatic ion thrusters.

Exploring the physics of low pressure plasmas expanding in a diverging magnetic nozzle plays an important role in the development of this new technology. While the design of RF plasma thrusters commonly include an antenna centred at the same location of the peak magnetic field (i.e. the location of main plasma excitation coincides with the magnetic nozzle throat), this study explores the effect of the input power on plasma expansion in a magnetic nozzle RF plasma thruster where the location of plasma generation is decoupled from the magnetic nozzle throat. The study of the plume ejected from a plasma thruster by means of intrusive plasma diagnostics is essential to evaluate its performance and study possible interactions with critical components of the spacecraft [22,23]. Two-dimensional measurements of the floating potential, ion saturation current, and ion energy distribution functions for increasing RF power are carried out with a set of custom-made plasma diagnostics. The probes (i.e., a Langmuir probe, an emissive probe and a retarding field energy analyser) are employed to characterise the plasma plume of the thruster, with particular focus on analysing plasma expansion and supersonic ion acceleration mechanisms for low-to-mid power level thruster applications.

2. Experimental apparatus

The experiments are conducted in *Moa*, a radio-frequency plasma device at The University of Auckland dedicated to the research of the physical processes that occur in magnetic nozzle radio-frequency plasma thrusters. A schematic of the apparatus is shown in Fig. 1(a). The plasma source comprises a 90 mm-diameter 0.5 mm-thick borosilicate glass tube, which connects through a custom-made vacuum flange to a 700 mm-long, 250 mm-radius vacuum chamber. The interface between the source and the chamber is defined as the centre of *Moa*'s coordinate system, i.e. $(r, z) = (0, 0)$ cm. *Moa* is pumped down using an Agilent TwisTorr 704FS turbo pump, which is backed up by a VRD-24 two-stage primary pump with a suction capacity of 24 m^3/h. This pumping system allows to reach a static pressure of $\sim 10^{-7}$ Torr ($\sim 10^{-5}$ Pa). During the experiments, the flow rate of argon is set at 12 sccm by the use of a mass flow controller to maintain a neutral pressure in the expansion chamber of 0.5 mTorr (70 mPa). This pressure is chosen to allow ion beam formation as its generation is hindered for pressures higher than 1 mTorr [24]. The plasma is excited by a 1.3 loop antenna, centred at $z = -18$ cm, through a water-cooled 1 kW RF power supply working at 27.12 MHz. Loop antennas are commonly employed in inductively-coupled discharges and can excite helicon waves with an $m = 0$ mode [25]. To maximise the power transfer from the RF generator using a custom-made L-type matching network, and the reflected power is consistently kept under 1% throughout the entire experimental campaign.

The plasma is created in the source and is then guided by the magnetic nozzle to the vacuum chamber, following the gradient of magnetic field strength, where it can expand mimicking the plasma expansion processes in space. A set of three skewed, concentric coils of increasing radius generates a convergent-divergent magnetic field of which intensity and orientation can be controlled by independently tuning the current input in each coil, and the location of the magnetic nozzle throat is at $z = -8$ cm. The solenoids are inclined by 15° with respect to the system axis z and precessed by an angle of 120° with respect to each other to create a rotational-symmetry arrangement. Further details on the system design can be found in [13,26]. Due to the complex 3D coil design, slight asymmetries of the magnetic field lines are present. However, they are negligible as they are maximum $\approx 2°$ on the $z - y$ plane at 10 cm downstream from the nozzle throat. A previous experimental campaign has also shown that the expanding radial plasma profile is not significantly affected by asymmetries in the magnetic field lines when the coils are operated in a symmetric magnetic nozzle configuration [26]. Fig. 1(b) shows the magnetic field on axis when all three coils are operated to generate a symmetric magnetic nozzle.

While the antenna is commonly placed at the same axial location as the coils, in this apparatus the location of plasma excitation ($z = -18$ cm) is decoupled from the magnetic nozzle throat (at $z = -8$ cm). The antenna and coils positions were set such that the magnetic field lines that intersect the antenna could freely escape the plasma source without crossing any physical boundaries.

2.1. Plasma diagnostics

Measurements of the floating potential V_f and the ion saturation current I_{sat} are carried out with a planar Langmuir Probe (LP) both in the plasma source and in the expansion chamber. The LP is constructed with a single-sided 2 mm diameter nickel disk biased at $V_{bias} = -80$ V with respect to ground to ensure total electron rejection and to measure I_{sat}. At each location, the reported I_{sat} is the average of the samples obtained from the data acquisition system with a sampling rate of 10^5 Samples/s and a scan time of 1 s. The same probe is kept floating to take measurements of the floating potential.

The plasma potential in the plasma source is measured using an emissive probe (EP). The probe consists of a 0.127 mm diameter tungsten wire bent to form a U-shape and subsequently inserted into a two-bore ceramic tube, where short pieces of tungsten wire are tightly fit into the bores to provide an electrical connection between the probe tip and the copper wires employed to transmit and read the signal. A DC power supply, isolated from ground using an isolation transformer, is used to heat the filament to allow electron emission. The respective I-V characteristics is found by sweeping the current I_{heat} from 1.6 to 2.6 A with a step increase of 0.025 A, and the local plasma potential is obtained by using the floating potential method [27,28]. The expected measurement error of V_p measured by the EP in *Moa* is ±2.75 V.

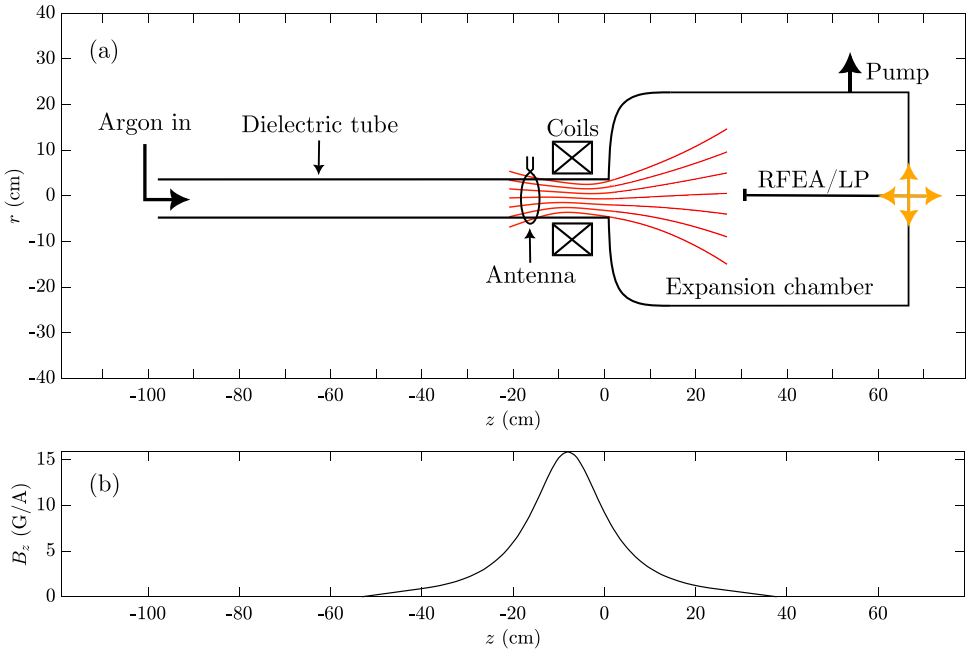

Fig. 1. (a) Schematic of the experimental set-up *Moa*. The orange arrows indicate the directions in which the probes can be moved. The solid red lines represent the magnetic field lines. The abbreviations RFEA/LP in the figure refer to the retarding field energy analyser and the Langmuir probe, respectively. (b) Magnitude of the magnetic field on axis B_z. (For interpretation of the references to colour in this figure legend, the reader is referred to the web version of this article.)

A four-grid retarding field energy analyser (RFEA) is used in ion collection mode to map the ion energy distribution function (IEDF) in the plasma plume, to measure the plasma and ion beam potentials, and the ion beam speed only in the expansion volume. The RFEA head consists of a grounded steel box with a 2 mm aperture to allow the particles' flux to enter. The box encloses four nickel grids attached to hollow copper plates using a vacuum-proof epoxy resin. The grids filter the flux of particles in terms of their energy. The nickel plate, called the collector plate, is placed behind the grid assembly and, as the name suggests, collects the current of ions passing through the RFEA. The nickel grids are namely the earth grid at potential 0 V, the repeller grid biased at −90 V, the discriminator grid and the secondary grid. The grids are formed by nickel micro-mesh sheets with hole sizes of ≈23 μm and having a transparency of 55%; they are electrically insulated from each other by a 0.1 mm thick polyimide sheet. By measuring the current which passes through the secondary grid and the collector plate, the IEDF, the local plasma potential and the ion beam energy can be inferred. The *I-V* characteristics of the ions are obtained by sweeping the discriminator grid voltage V_D from 0 to 80 V. The biasing voltage of the RFEA is defined by several periods of a triangle wave function with a sweeping frequency of 15 Hz. The collected current is deduced by measuring the voltage drop across a resistor R_M with an operational amplifier, and each measured current is the average of 200 V_D sweeps. An analogue differentiator is used to obtain the first derivative of the *I-V* current and estimate the local plasma potential V_p and the ion beam potential V_B from the location of the first and second peak of the ion energy distributions, respectively [13,15,18,29]. An error of ±2 V on measurements of the plasma and beam potentials is estimated. A detailed description of the analogue differentiator and of the data processing techniques used to evaluate the IEDF can be found in [30].

3. Results & discussion

The data reported in this study are collected at an argon flow rate of 12 sccm and feed pressure of 0.5 mTorr (≈70 mPa), and a maximum magnetic field on axis of $B_{z,max}$ = 340 G. The RF input power is steadily increased from 100 W to a maximum of 400 W. The maximum power configuration achievable was limited by the extensive heating of the copper loop antenna at higher power levels.

3.1. Mode transition

The power transfer efficiency η_{RF} can be used to quantify the antenna/plasma coupling in *Moa*, and it is defined as

$$\eta = \frac{P_{abs}}{P_{RF}} = \frac{R_p}{R_p + R_{ant}}, \quad (1)$$

where P_{abs} is the power absorbed by the plasma, P_{RF} is the input power from the RF power supply (i.e. 250 W), R_p is the plasma resistance and R_{ant} = 0.34 Ω is the circuit resistance (antenna + coax cables + *I-V* probe). An *Octiv*™ Suite *I-V* probe was used to measure the plasma resistance R_p. The behaviour of the power transfer efficiency can be compared to the variation of the ion saturation current, which can be used as a proxy for plasma density, to better analyse the influence of power input on the plasma production. Fig. 2(a) shows the value of the ion saturation current on axis for RF power inputs ranging from 100 W to 400 W for a fixed magnetic field strength and argon pressure. Similarly, the power transfer efficiency as a function of increasing RF power input is plotted in Fig. 2(b). As expected, both plots exhibit a similar increasing trend. The power transfer efficiency increases with increasing RF power, which in turn results in a higher ionisation efficiency, and thus a greater plasma density. The biggest rise in η_{RF} is measured between 100 W and 200 W, with η_{RF} increasing of 10%. At higher powers, the rate of increase in power transfer efficiency gradually decreases and η_{RF} starts to plateau for power inputs P_{RF} > 250 W.

While no distinctive mode jumps can be observed, a characteristic feature of the transfer efficiency profile is the non-monotonic dependence of η with P_{RF}. Similar profiles of a steady rise of power input coupled by a slowdown in the growth of the ion current measured in an RF inductive plasma source have been reported in other studies [31–33].

It is currently hypothesised that the discharge undergoes a mode change from capacitively couple (CCP) to inductively coupled (ICP) for RF powers greater than 200 W. The minimum plasma density required to sustain a specific coupling mode is determined by the balance between the absorbed and lost power. Therefore, if the plasma density is high enough even in a CCP discharge, a mode transition can occur

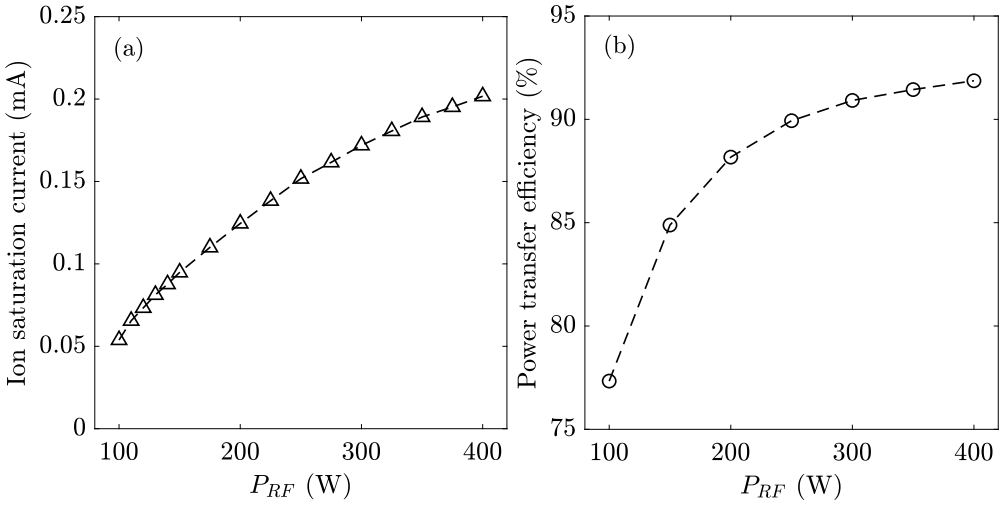

Fig. 2. Plot of the ion saturation current (a) and the power transfer efficiency η_{RF} (b) measured in *Moa* as a function of the power input P_{RF}.

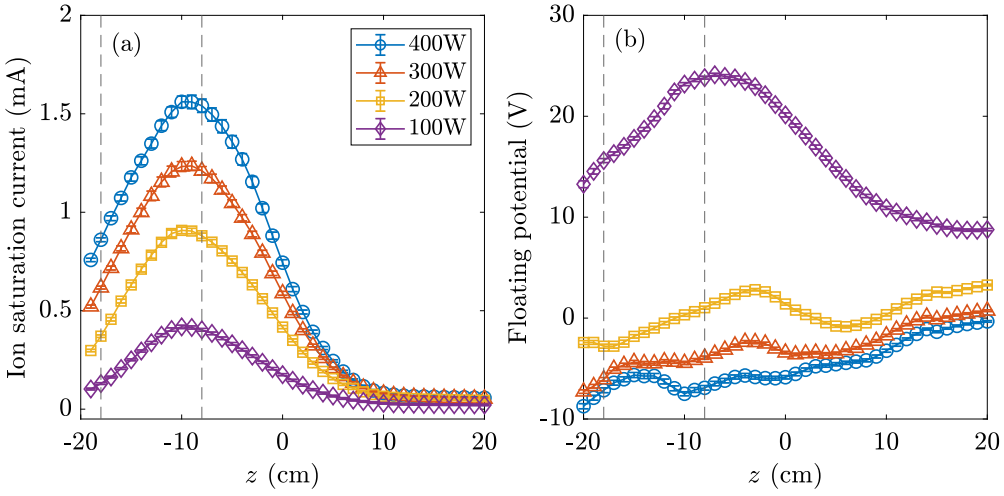

Fig. 3. Axial profile of the ion saturation current I_{sat} (a) and of the floating potential V_f (b) measured for increasing RF power input. It can be noted that the error bars are smaller than the marker size for all of the data sets.

without a sharp change in density [34]. In the CCP region, the density would increase significantly because of the greater heating region inside a skin layer of size comparable to the characteristic length of the plasma source. With the further increase of the density, the size of the skin depth decreases, leading to a reduction of the inductive coupling efficiency. The E-H mode transition from a CCP to an ICP discharge would also help explain the different plasma profiles measured for $P_{RF} = 100$ W and the ones obtained at the higher power configurations. These will be discussed in more details in the following sections.

3.2. Effect of input power on ion saturation current and floating potential

To qualitatively assess the effect of power input on plasma density in the device, spatial measurements of the ion saturation current were carried out both in the plasma source and in the expansion chamber. Fig. 3(a) shows the axial profiles of I_{sat} for increasing RF power. The collected ion current at 400 W was six times higher under the antenna, and three times higher at the magnetic nozzle throat when compared to I_{sat} measured at the lowest power level. The significant density growth observed as the power is increased can be explained by the rise of the power transfer efficiency with P_{RF} discussed earlier. An interesting feature worth noting of the axial ion current profiles is the location of the I_{sat} maxima. The peak does not occur at the point of plasma excitation (i.e., under the antenna), but 2 cm upstream of the magnetic nozzle throat. This feature has been observed in other experiments [13,20,35] and it is hypothesised to be caused by downstream local ionisation caused by high-energy electrons travelling along the field lines. The axial profile of the floating potential plotted in Fig. 3(b) shows a significantly different trend between the data collected at 100 W and the one measured at higher power levels. While for the lowest RF power value V_f is positive all along the axis, the potential becomes progressively more negative as the power is increased above 100 W, with minima localised under the antenna's region. Since significant negative values of V_f compared to the plasma potential could be a sign of the presence of high-energy electrons, the floating potential profiles for $P_{RF} > 100$ W suggest that an enhanced power deposition might take place along the axis as the power input increases.

Two-dimensional measurements of the plasma plume were carried out with the Langmuir probe both in the plasma source and expansion volume to link the upstream and downstream plasma conditions. Fig. 4 shows the contour plots of the ion saturation current and of the floating potential for increasing power input P_{RF}. The data has been mirrored for visual clarity around $r = 0$ cm, as previous radial measurements showed a symmetric structure around the axis. As can be seen, a hollow ion saturation current profile is present in all of the power configurations analysed. It is also noticed that the field lines encompassing the

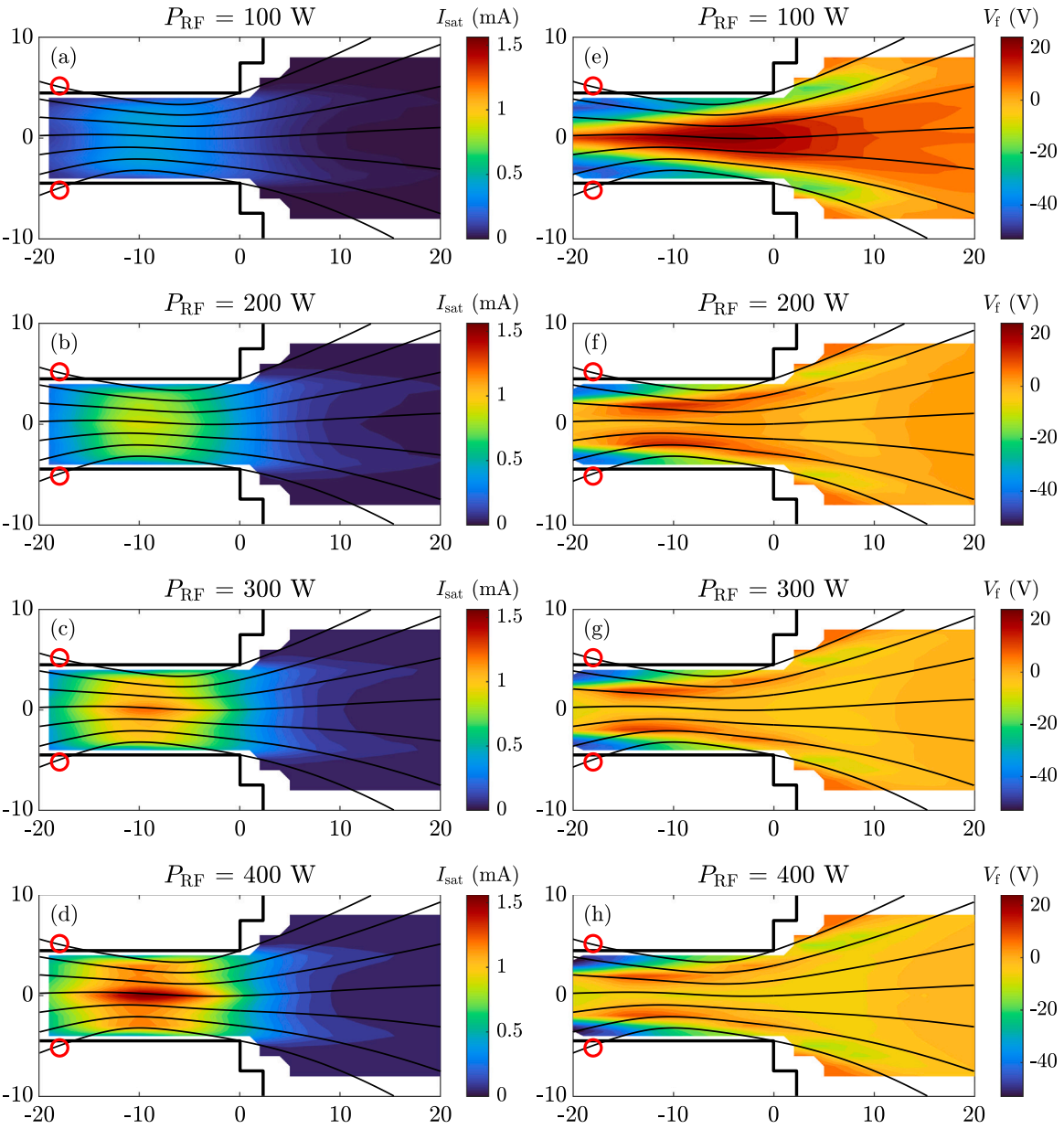

Fig. 4. 2-Dimensional profiles of the ion saturation current I_{sat} (a–d), and of the floating potential V_f (e–h) measured for increasing RF power input P_{RF}. The red circles indicate the antenna centred at $z = -18$ cm. The solid black lines represent the magnetic field lines. (For interpretation of the references to colour in this figure legend, the reader is referred to the web version of this article.)

conics are always the most radial field lines that leave the source and intersect the antenna upstream. A similar behaviour has been reported in other experiments [36–39]. In plots (e–h) of Fig. 4, a region of negative floating potential is also observed to exist along the same radial magnetic field lines that reconnect to the main excitation region, with V_f becoming progressively more negative under the antenna.

The plasma plume evolution during the expansion phase can be better understood by taking radial slices of the 2-D maps shown in Fig. 4 at specific axial locations. Figs. 5(a) and 6(a) show the radial profiles of the ion saturation current measured at the magnetic nozzle throat and downstream at $z = 9$ cm, respectively. As expected, higher I_{sat} values are collected for increasing power input in both axial locations, indicative of greater plasma densities. However, the radial current profiles exhibit a notable difference. While I_{sat} has a maximum on axis for $P_{RF} > 100$ W and then decreases radially in the plasma source, a double-peaked profile forms downstream with maxima at $r = \pm 4.5$ cm for all RF power configurations (see Fig. 6(a)).

The same feature, called high-density conics, has been previously observed in the device when studying the effect of magnetic field strength on plasma expansion [13]. Numerous studies have reported a hollow density structure forming in the magnetic nozzle [36–46]. Two mechanisms have been identified so far that could be the cause for the generation of the conics: (1) off-axis local ionisation occurring downstream of the MN, and (2) peripheral trapping of ions by a radial potential well caused by highly magnetised electrons [45,46].

Fig. 7 shows the radial plasma potential profile measured at the location of the high-density conics. As it can be seen, V_p exhibits an axial peak and then decreases radially, setting up a radial electric field of $E_r \sim 1$ V/cm for $P_{RF} > 100$ W. The profile measured at the lowest power configuration is different, showing a plateau between $-4 < r < 4$ cm followed by a potential drop in the order of ~0.6 V/cm. As mentioned earlier, some studies discussed the hypothesis of radial plasma density accumulation and simultaneously reported a radial potential well in the plume that would radially trap the ions [45,46]. Particularly, [46]

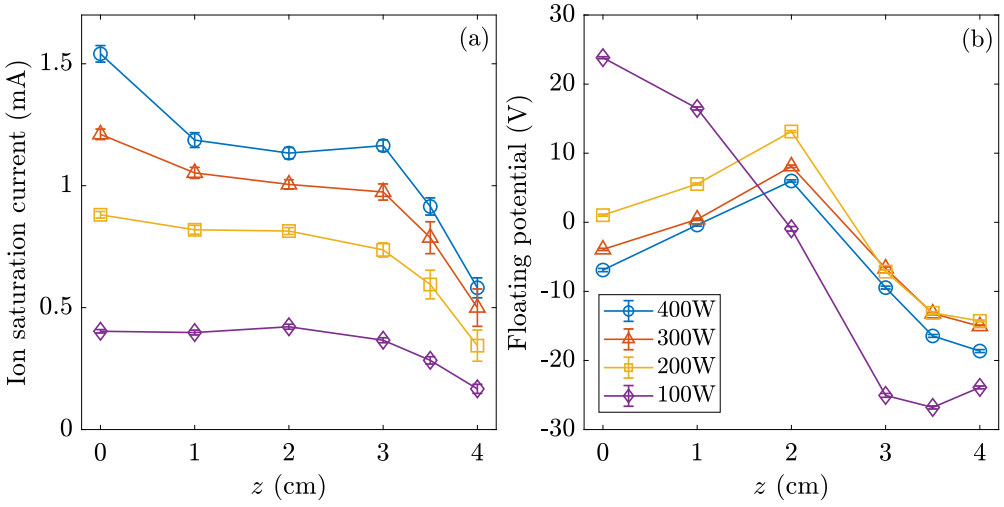

Fig. 5. Radial profile of the ion saturation current I_{sat} (a) and of the floating potential V_f (b) measured at the magnetic nozzle throat $z = -8$ cm for increasing RF power input. It can be noted that the error bars are smaller than the marker size for most of the data sets.

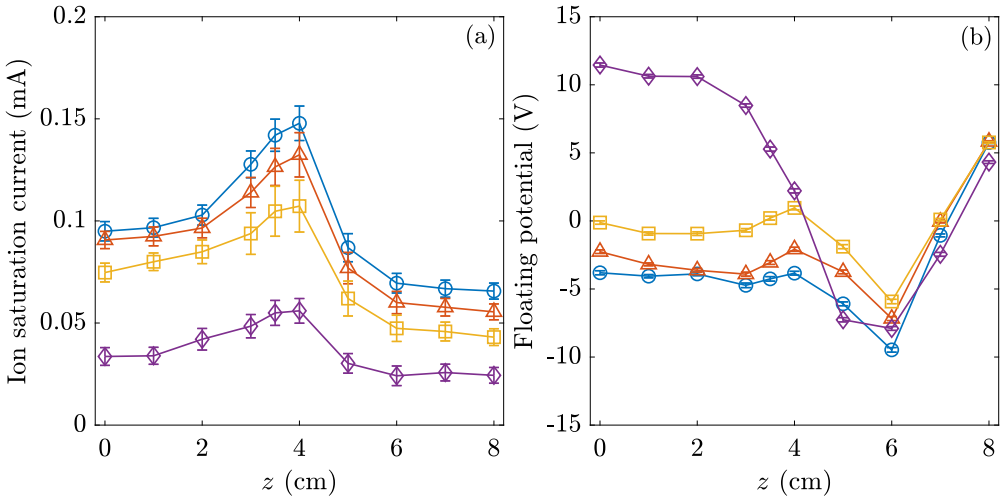

Fig. 6. Radial profile of the ion saturation current I_{sat} (a), and of the floating potential V_f (b) measured at $z = 9$ cm for $P_{RF} = 100$ W (red diamonds), $P_{RF} = 200$ W (green squares), $P_{RF} = 300$ W (orange triangles), and $P_{RF} = 400$ W (blue circles). It can be noted that the error bars are smaller than the marker size for the floating potential profiles.

assumed a fully ionised, collisionless and highly-magnetised plasma that is far from the plasma conditions in *Moa*. The relatively weak magnetic field used in the experimental campaign would be incapable of trapping enough ions along the plume edge. This is further supported by the fact that no potential well has been observed downstream of the magnetic nozzle, where no radial V_p local minima have been measured.

The theory of peripheral local ionisation has been discussed in numerous studies [13,36,37,39–44] where a high-energy electron tail with energies higher than the gas ionisation energy has been measured along the most radial field lines reconnecting with the antenna. The radial profile of the floating potential, plotted in Fig. 6(b), shows regions of minima of floating potential on the same radial locations of I_{sat} maxima, which could be associated with the off-axis presence of high-energy electrons. The downstream transport of this high-energy electron population created under the antenna along the most radial field lines would then contribute to local ionisation, generating the hollow density structure observed [36,37,40,47].

3.3. Axial characterisation of the ion beam

As mentioned in Section 2, the retarding field energy analyser was used to detect the characteristics of the ion beam in the plume of *Moa*. Fig. 8 shows the ion energy distribution functions measured on axis for increasing RF power at two different locations. For all the power configurations analysed, two populations of ions are detected: a higher energy one corresponding to the accelerated ions at potential $V_B \sim 30$ V, and a lower energy population corresponding to the background ions at the local plasma potential $V_p \sim 20$ V. In a collisional plume, the term 'background thermal ions' refer to the ions at the local plasma potential V_p that are created by a combination of ionisation and ion-neutral charge-exchange collisions between the beam ions exited in the source and the neutrals present downstream. This definition is used in numerous other studies [15,17,29,39,48]. Comparing the IEDFs measured in the plume at $z = 5$ cm and at $z = 9$ cm in Fig. 8, it can be seen that the peak corresponding to the low-energy ion population becomes more prominent as the RFEA is moved along the axis, while the accelerated ion beam component decreases. The ion-neutral mean free path for charge-exchange and elastic collisions for the neutral pressure under analysis is comparable to the distance between the source exit and the probe position i.e., $\lambda_{mfp} \sim 10$ cm. The fast ions would then collide with the neutrals as the RFEA covers the axial distance of the measurements. This is shown by the increase in amplitude of the ion energy distribution function near the plasma potential as the plasma expands, and the corresponding decrease in the ion beam component.

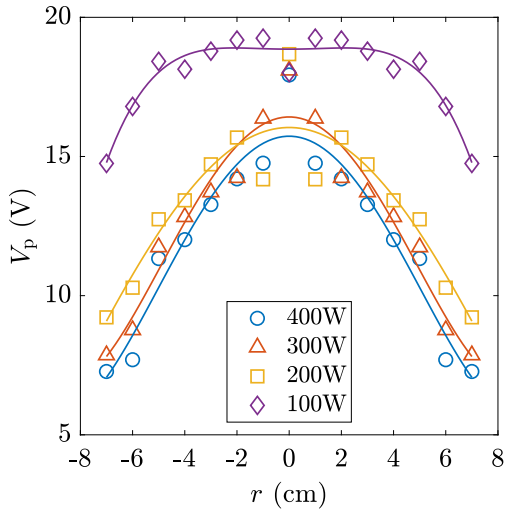

Fig. 7. Radial profile of the plasma potential V_p measured in the plume at $z = 9$ cm for $P_{RF} = 100$ W (red diamonds), $P_{RF} = 200$ W (green squares), $P_{RF} = 300$ W (orange triangles), and $P_{RF} = 400$ W (blue circles). The data has been mirror around $r = 0$ cm for visual clarity.

While the value of ion beam potential (i.e., the location of the second IEDF peak) stays approximately constant as the probe moves downstream from $z = 5$ cm to $z = 9$ cm (as summarised in Table 1), the plasma potential decreases along the axis. This is expected since the plasma undergoes a Boltzmann-like expansion. This behaviour is visible in Fig. 9, which shows the plasma and ion beam potentials along the axis as the RF power is increased. As shown in Fig. 9(a), the plasma potential decreases along the axis as the plasma expands. The ensuing ambipolar electric field would then act to accelerate ions downstream of the nozzle. It is interesting to note that the smallest potential drop ΔV is measured for $P_{RF} = 100$ W, while further increasing the power input appears not to affect the magnitude of ΔV. The axial profiles of the plasma potential also exhibit a plateau for $z > 10$ cm.

Fig. 10(a) shows the total ion current I_{tot}, defined at the current measured as $V_D = 0$ V, measured on axis with the RFEA for increasing power. The profiles match well the ion saturation current behaviour obtained with the Langmuir probe as discussed earlier. However, it is noted that I_{tot} is much smaller than the ion current measured by the LP. This can be explained by the fact that the RFEA only collects ions that fall through the probe sheath with an acceptance angle of ±40°, thus the measured current would be lower than the LP data as some of the ions would not be detected. A further reduction in the collected ion current would be caused by the reduction in the effective combined transparency of the four nickel grids due to misalignment during the assembly. Another contribution to the discrepancy observed between the ion current measured by the two probes could be related to the fact that I_{sat} obtained with the Langmuir probe is not always constant, especially at very negative biasing voltages, and the I–V characteristics would typically exhibit a slope in the ion saturation region [49].

The axial profiles of the ion beam current I_B measured for the different RF power configurations are shown in Fig. 10(b). The ion beam current I_B can be used to qualitatively assess the beam density. I_B can be obtained from the I-V curve and is defined as the current measured at the beam potential, i.e. $I_B = I_C(V_B)$ [50,51]. It is important to note that the ion beam current I_B at potential V_B is a measurement of all the ions possessing an energy $\varepsilon_B \geq qV_B$. Hence, the other part of the ion beam population having an energy $\varepsilon_B < qV_B$ is not accounted for. For the purposes of this study, this definition of the ion beam current is sufficient to qualitatively assess the density of the accelerated ion population. The profiles of both the total ion current and the ion beam current in Fig. 10 show a similar behaviour. As expected, the value of the measured currents increases for increasing power input, and it decreases along the axis as a result of plasma expansion and ion-neutral charge-exchange collisions.

Table 1
Average ion beam potential $V_{B,avg}$ and maximum ion beam speed $v_{B,max}$ as a function of RF power.

P_{RF} (W)	$V_{B,avg}$ (V)	$v_{B,max}$ (km/s)
100	32.9	9.5
200	30.4	11.4
300	31.8	11.7
400	33.3	12.0

3.3.1. Detection of a supersonic ion beam

The ion beam speed v_B on axis can estimated from the following equation,

$$v_B = \sqrt{\frac{2\varepsilon_B}{m_i}} = \sqrt{\frac{2e(V_{B,avg} - V_p)}{m_i}}, \quad (2)$$

where $\varepsilon_B = e(V_B - V_p)$ is the energy of the beam [18,29,52]. Thus, the larger the overall potential drop, the higher the ion beam velocity. The value of the ion beam potential (obtained with the RFEA) is ideally constant along the axis since the high-speed ion population would retain its original energy imparted by the acceleration potential, i.e. V_B is equal to the value of plasma potential where the potential drop begins. [13]. As it can be observed from Fig. 9(b), this is indeed the case and the average value of ion beam potential can be used in the calculation of the ion beam speed. It should be noted that the values of plasma potential used to calculate the ion speed for $z < 0$ cm were measured using an emissive probe since the size of the RFEA head would have perturbed the plasma within the source volume, while the plasma potential values in the plume were obtained from the post-processing of the ion energy distribution function. Fig. 11 shows the magnitude of v_B on axis as a function of input power obtained from Eq. (2).

Table 1 summarises the average ion beam potential $V_{B,avg}$ and maximum ion beam speed $v_{B,max}$ measured for the different RF power configurations. As the ion sound speed in the system is $c_S \sim 4$ km/s for an electron temperature of $T_e = 6$ eV [13], the maximum ion Mach number ($M = v_B/c_S$) is estimated to range from $M = 2.5$ for $P_{RF} = 100$ W ($v_{B,max} \sim 9.5$ km/s), to $M = 2.7$ for the other power configurations ($v_{B,max} \sim 12$ km/s). As expected, the ion beam is accelerated to supersonic speeds by the ambipolar electric field for all of the power configurations studied, and the speed value is observed to plateau as the plasma expands. Interestingly, while the smallest potential drop was measured for the lowest power case, increasing the power level from 200 W to 400 W did not modify the magnitude of the axial electric field, and similar ion beam speeds are predicted for $P_{RF} > 100$ W.

It should be noted that in reality the electron temperature used in the estimation of the ion sound speed would not be constant but it would vary under different power conditions and along the axis while the plasma expands. Due to the unavailability at the moment of the experimental campaign of an RF compensated Langmuir probe, reliable measurements of the electron temperature could not be taken. In the *Moa* device, the effective electron temperature can be estimated from the Boltzmann relation and ranges from 6 eV (at $P_{RF} = 100$ W) to 8 eV (at $P_{RF} = 200 - 400$ W) for the experimental conditions analysed. Variations of the effective electron temperature along the axis can be estimated from the relation $V_p - V_f \approx 5.2T_e$ for argon [25,51,53], which would result in an axial decrease of $T_{e,eff} \approx 2$ eV. Since the ion sound speed is proportional to the square root of T_e ($c_s = \sqrt{qT_e/m_1}$), c_s is 'weakly' influenced by variations in T_e. Indeed, for a $T_e = 6$ eV the resultant $c_s = 3.8$ km/s, while for $T_e = 8$ eV the resultant $c_s = 4.4$ km/s.

Comparable ion beam speeds and plateau behaviour were observed in similar experiments [10,15,18]. It is interesting to note that, contrary

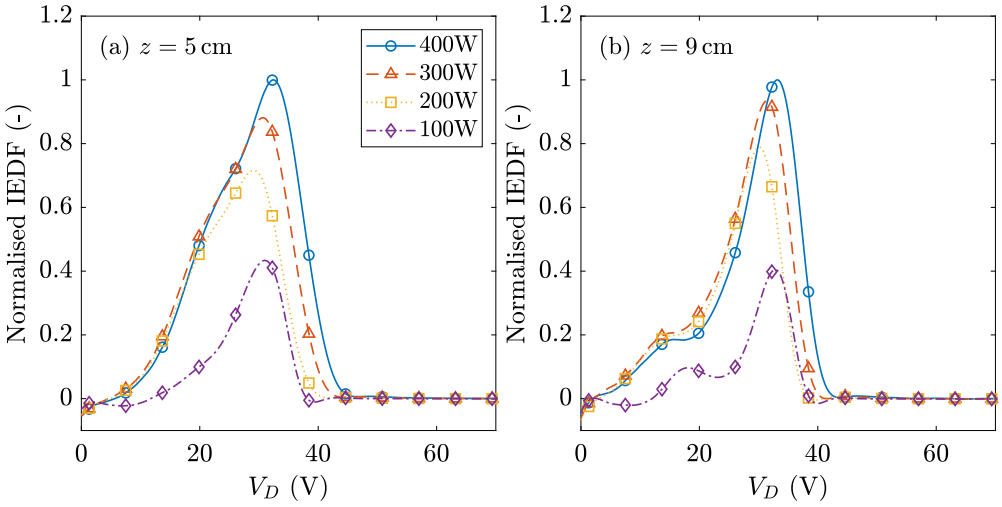

Fig. 8. Ion energy distribution functions measured on axis at $z = 5$ cm (a) and at $z = 9$ cm (b). The IEDFs are normalised by the peak measured at each axial location for $P_{RF} = 400$ W.

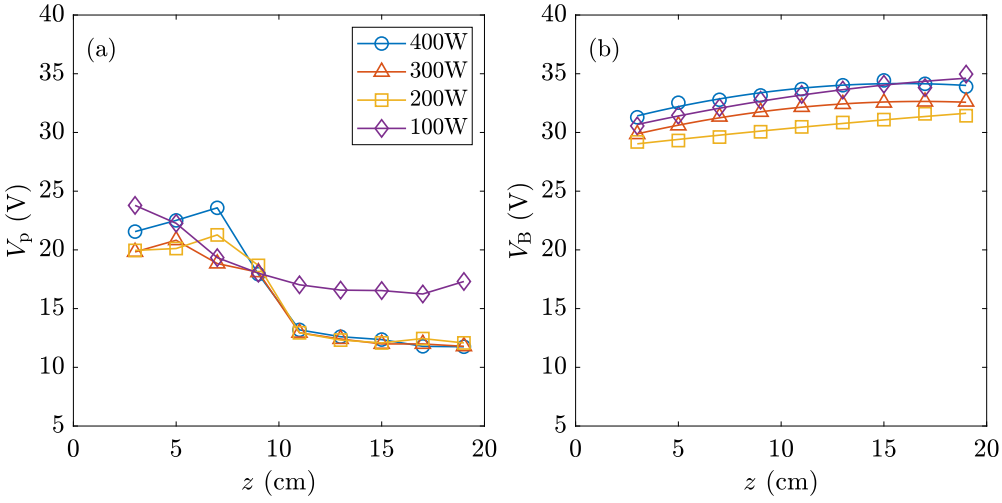

Fig. 9. Axial profile of the plasma potential V_p (a) and ion beam potential V_B (b) for increasing RF power input. The estimated error in the measurements is ±2 V.

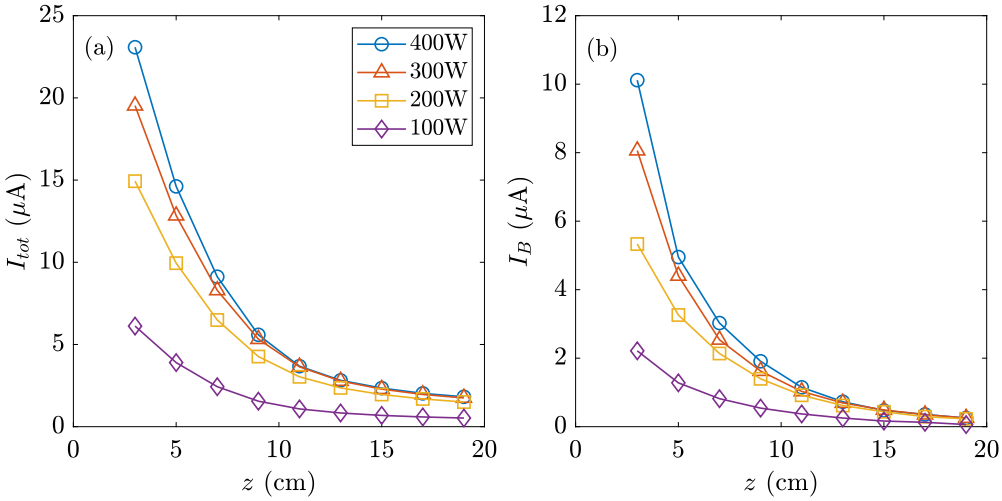

Fig. 10. Axial profile of the total ion current I_{tot} (a) and ion beam current I_B (b) for increasing RF power input.

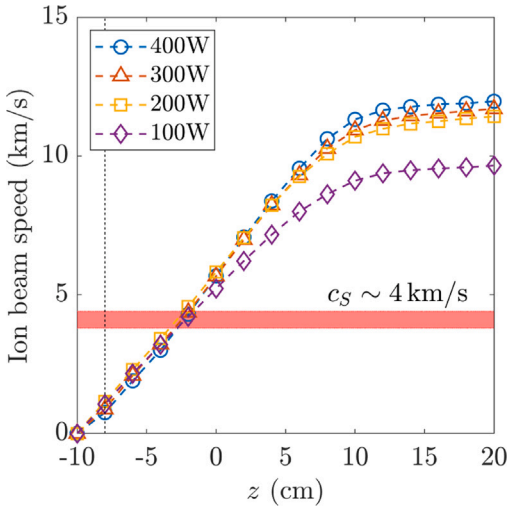

Fig. 11. Ion beam speed v_B on axis for increasing RF power input. The red shaded area marks the region of ion sound speed $c_S \sim 4$ km/s for an electron temperature ranging from $T_e = 6$ eV to $T_e = 8$ eV. The vertical dotted line at $z = -8$ cm shows the location of the magnetic nozzle throat. The average error in v_{beam} is estimated to be ±800 m/s.

to the idealised physical model, the ion sonic transition where $v_B > c_S$ is not localised at the magnetic nozzle throat, but it is observed to move downstream ($z > -8$ cm) for all the RF power cases. It can be seen from the plot that it occurs close to the geometrical expansion point at $z = -2$ cm, i.e. near the interface between the source tube and the expansion chamber. While increasing input power appears not to affect the location where $v_B > c_S$, a previous experimental campaign, which studied the effect of magnetic nozzle strength in the *Moa* plasma device, reported that the location of ion sonic transition was affected by the magnitude of the magnetic field, and that it moved progressively further downstream from the MN throat as the field strength was increased [54].

The reason for this behaviour is still unclear, and further studies are required. Correyero et al. (2018) [55] and Collard and Jorns (2019) [56] have also observed the location at which ions are accelerated to supersonic speeds to be shifted with respect to the MN throat. This resulted in a reduced performance since the expansion ratio was effectively reduced as the ion sonic transition moved downstream. It was suggested that the shifting of the nozzle throat could partly be a result of ion-neutral charge-exchange collisions, which would act as a drag term on the subsonic ions, delaying their acceleration [56].

4. Conclusions

The effect of input power on plasma expansion and ion acceleration in a magnetic nozzle were analysed in a radio-frequency (RF) plasma device where the location of plasma generation is decoupled from the nozzle throat. The data reported was collected at an argon pressure of 0.5 mTorr (≈70 mPa) and a maximum magnetic field on axis of $B_{z,max} = 340$ G. The RF input power was increased from 100 W to a maximum of 400 W.

The non-monotonic dependence of the power transfer efficiency on the ion saturation current hints to the existence of a mode jump occurring in the plasma device for a fixed magnetic field strength and argon pressure. It is currently believed that the plasma transitions from a capacitively coupled to an inductively coupled discharge for RF powers greater than 200 W. This behaviour would help explain the different ion density and potential profiles measured for $P_{RF} = 100$ W when compared to the plasma characteristics collected for $P_{RF} = 200 - 400$ W. However further studies are necessary to clearly understand the influence of coupling mode on the plume characteristics.

Measurements of the ion saturation current and of the ion beam current showed that the plasma density and the ion beam density increased for increasing power input. This was expected since the power transfer efficiency was observed to increase as a function of RF power. The 2-D profiles of the ion saturation current also showed the formation of high-density conics in the plasma plume, which radial maxima matched the location of minima of the floating potential. This hollow density structure is hypothesised to be the result of local downstream ionisation caused by the transport of high-energy electrons along the most radial field lines leaving the source tube.

While the smallest potential drop was measured for the lowest power case, increasing the power level from 200 W to 400 W did not modify the magnitude of the axial electric field, and similar ion beam speeds are predicted for $P_{RF} > 100$ W, with the maximum ion Mach number ranging from $M = 2.5$ for $P_{RF} = 100$ W ($v_{B,max} \sim 9.5$ km/s), to $M = 2.7$ for the other power configurations ($v_{B,max} \sim 12$ km/s). The most interesting feature observed was the point of the ion sonic transition where $v_B > c_S$. For all the power levels analysed, the ions accelerated by the ambipolar electric field reach sonic speeds not at the magnetic nozzle throat, but further downstream ($z > -8$ cm), close to the geometrical expansion point ($z \approx 0$ cm).

CRediT authorship contribution statement

Antonella Caldarelli: Writing – review & editing, Writing – original draft, Visualization, Validation, Methodology, Investigation, Formal analysis, Data curation, Conceptualization. **Raoul Andriulli:** Writing – review & editing, Writing – original draft, Methodology, Investigation, Formal analysis, Data curation. **Fabrizio Ponti:** Writing – review & editing, Supervision, Resources. **John Cater:** Writing – review & editing, Supervision, Project administration, Funding acquisition. **Nicholas Rattenbury:** Writing – review & editing, Supervision, Project administration, Funding acquisition.

Declaration of competing interest

The authors declare that they have no known competing financial interests or personal relationships that could have appeared to influence the work reported in this paper.

References

[1] P.G. Sutton, O. Biblarz, Rocket Propulsion Elements, ninth ed., John Wiley and Sons, Inc., New York, 2017, pp. 671–689, Ch. 18.
[2] European Space Agency, Electric blue thrusters propelling BepiColombo to Mercury, 2018, (Accessed 30 August 2023).
[3] C. Charles, P. Alexander, C. Costa, O. Sutherland, R. Boswell, L. Pfitzner, R. Franzen, J. Kingwell, A. Parfitt, P.-E. Frigot, J. Gonzalez del Amo, E. Gengembre, Helicon double layer thruster, in: 42nd AIAA/ASME/SAE/ASEE Joint Propulsion Conference and Exhibit, 2006, http://dx.doi.org/10.2514/6.2006-4838.
[4] E. Ahedo, J. Navarro-Cavallé, Helicon thruster plasma modeling: Two-dimensional fluid-dynamics and propulsive performances, Phys. Plasmas 20 (4) (2013) 043512, http://dx.doi.org/10.1063/1.4798409.
[5] T. Lafleur, Helicon plasma thruster discharge model, Phys. Plasmas 21 (4) (2014) 043507, http://dx.doi.org/10.1063/1.4871727.
[6] K. Takahashi, Helicon-type radiofrequency plasma thrusters and magnetic plasma nozzles, Rev. Mod. Plasma Phys. 3 (2019) 044510, http://dx.doi.org/10.1007/s41614-019-0024-2.
[7] K. Takahashi, T. Sugawara, A. Ando, Spatial measurement of axial and radial momentum fluxes of a plasma expanding in a magnetic nozzle, New J. Phys. 22 (7) (2020) 073034, http://dx.doi.org/10.1088/1367-2630/ab98d5.
[8] W. Cox, C. Charles, R.W. Boswell, R. Laine, M. Perren, Magnetic ion beam deflection in the helicon double-layer thruster, J. Propuls. Power 26 (5) (2010) 1045–1052, http://dx.doi.org/10.2514/1.49202.
[9] M. Merino, E. Ahedo, Contactless steering of a plasma jet with a 3D magnetic nozzle, Plasma Sources Sci. Technol. 26 (2017) 095001, http://dx.doi.org/10.1088/1361-6595/aa8061.
[10] R. Imai, K. Takahashi, Deflections of dynamic momentum flux and electron diamagnetic thrust in a magnetically steered rf plasma thruster, J. Phys. D: Appl. Phys. 55 (13) (2022) 135201, http://dx.doi.org/10.1088/1361-6463/ac4451.

[11] R. Imai, K. Takahashi, Demonstrating a magnetic steering of the thrust imparted by the magnetic nozzle radiofrequency plasma thruster, Appl. Phys. Lett. 118 (2021) 264102, http://dx.doi.org/10.1063/5.0058202.
[12] K. Takahashi, R. Imai, Two-dimensional deflection of a plasma plume exhausted from a magnetically steered radiofrequency plasma thruster, Phys. Plasmas 29 (5) (2022) 054501, http://dx.doi.org/10.1063/5.0090476.
[13] A. Caldarelli, F. Filleul, R.W. Boswell, C. Charles, J.E. Cater, N.J. Rattenbury, Effects of magnetic nozzle strength and orientation on radio-frequency plasma expansion, Plasma Sources Sci. Technol. 32 (7) (2023) 075002, http://dx.doi.org/10.1088/1361-6595/ace1a6.
[14] C. Charles, R.W. Boswell, Current-free double-layer formation in a high-density helicon discharge, Appl. Phys. Lett. 82 (9) (2003) 1356–1358, http://dx.doi.org/10.1063/1.1557319.
[15] C. Charles, R.W. Boswell, Laboratory evidence of a supersonic ion beam generated by a current-free "helicon" double-layer, Phys. Plasmas 11 (4) (2004) 1706–1714, http://dx.doi.org/10.1063/1.1652058.
[16] W. Cox, C. Charles, R.W. Boswell, R. Hawkins, Spatial retarding field energy analyzer measurements downstream of a helicon double layer plasma, Appl. Phys. Lett. 93 (7) (2008) 071505, http://dx.doi.org/10.1063/1.2965866.
[17] Y. Zhang, C. Charles, R.W. Boswell, Effect of radial plasma transport at the magnetic throat on axial ion beam formation, Phys. Plasmas 23 (8) (2016) 083515, http://dx.doi.org/10.1063/1.4960828.
[18] A. Bennet, C. Charles, R.W. Boswell, In situ electrostatic characterisation of ion beams in the region of ion acceleration, Phys. Plasmas 25 (2) (2018) 023516, http://dx.doi.org/10.1063/1.5017049.
[19] A.E. Vinci, S. Mazouffre, Direct experimental comparison of krypton and xenon discharge properties in the magnetic nozzle of a helicon plasma source, Phys. Plasmas 28 (3) (2021) 033504, http://dx.doi.org/10.1063/5.0037117.
[20] F. Filleul, A. Caldarelli, C. Charles, R.W. Boswell, N. Rattenbury, J.E. Cater, Characterization of a new variable magnetic field linear plasma device, Phys. Plasmas 28 (12) (2021) 123514, http://dx.doi.org/10.1063/5.0070924.
[21] K. Takahashi, Thirty percent conversion efficiency from radiofrequency power to thrust energy in a magnetic nozzle plasma thruster, Sci. Rep. 12 (2022) 18618, http://dx.doi.org/10.1038/s41598-022-22789-7.
[22] C. Cai, Numerical studies on plasma plume flows from a cluster of electric propulsion devices, Aerosp. Sci. Technol. 41 (2015) 134–143, http://dx.doi.org/10.1016/j.ast.2014.12.018.
[23] Z. Zhang, Z. Zhang, S. Xu, W.Y.L. Ling, J. Ren, H. Tang, Three-dimensional measurement of a stationary plasma plume with a Faraday probe array, Aerosp. Sci. Technol. 110 (2021) 106480, http://dx.doi.org/10.1016/j.ast.2020.106480.
[24] A. Bennet, Low Pressure Plasmas in Magnetic Nozzles (Ph.D. thesis), Australian National University, 2019.
[25] P. Chabert, N. Braithwaite, Physics of Radio-Frequency Plasmas, first ed., Cambridge University Press, 2011.
[26] A. Caldarelli, F. Filleul, C. Charles, R.W. Boswell, N. Rattenbury, J.E. Cater, Radial characterization of an ion beam in a deflected magnetic nozzle, J. Electr. Propuls. 1 (10) (2022) 10, http://dx.doi.org/10.1007/s44205-022-00012-z.
[27] J.P. Sheehan, N. Hershkowitz, Emissive probes, Plasma Sources Sci. Technol. 20 (6) (2011) 063001, http://dx.doi.org/10.1088/0963-0252/20/6/063001.
[28] J.P. Sheehan, Y. Raitses, N. Hershkowitz, M. McDonald, Recommended practice for use of emissive probes in electric propulsion testing, J. Propuls. Power 33 (3) (2017) 614–637, http://dx.doi.org/10.2514/1.B35697.
[29] C. Charles, Hydrogen ion beam generated by a current-free double layer in a helicon plasma, Appl. Phys. Lett. 84 (3) (2004) 332–334, http://dx.doi.org/10.1063/1.1643548.
[30] A. Caldarelli, F. Filleul, R.W. Boswell, C. Charles, N.J. Rattenbury, J.E. Cater, Data processing techniques for ion and electron-energy distribution functions, Phys. Plasmas 30 (4) (2023) 040501, http://dx.doi.org/10.1063/5.0133840.
[31] M.A. Lieberman, R.W. Boswell, Modeling the transitions from capacitive to inductive to wave-sustained rf discharges, J. Physique IV 08 (1998) 145–164, http://dx.doi.org/10.1051/jp4:1998712.
[32] T. Zhang, K. Jiang, Z. Liu, L. Yang, H. Zhang, J. Ouyang, Q. Chen, Characteristics of inductively coupled plasma (ICP) and helicon plasma in a single-loop antenna, Plasma Sci. Technol. 22 (8) (2020) 085405, http://dx.doi.org/10.1088/2058-6272/ab8551.
[33] I. Zadiriev, E. Kralkina, K. Vavilin, A. Nikonov, G. Shvidkiy, Comparison of pulse-modulated and continuous operation modes of a radio-frequency inductive ion source, Plasma Sci. Technol. 25 (2) (2023) 025405, http://dx.doi.org/10.1088/2058-6272/ac8fca.
[34] S.-H. Seo, C. Chung, H.-Y. Chang, Review of heating mechanism in inductively coupled plasma, Surf. Coat. Technol. 131 (1) (2000) 1–11, http://dx.doi.org/10.1016/S0257-8972(00)00770-2, Proceedings of the 2nd Asian-European International Conference on Plasma surface Engineering.
[35] A. Bennet, C. Charles, R.W. Boswell, Non-local plasma generation in a magnetic nozzle, Phys. Plasmas 26 (7) (2019) 072107, http://dx.doi.org/10.1063/1.5098484.
[36] C. Charles, High density conics in a magnetically expanding helicon plasma, Appl. Phys. Lett. 96 (5) (2010) 051502, http://dx.doi.org/10.1063/1.3309668.
[37] K. Takahashi, H. Akahoshi, C. Charles, R.W. Boswell, A. Ando, High temperature electrons exhausted from rf plasma sources along a magnetic nozzle, Phys. Plasmas 24 (8) (2017) 084503, http://dx.doi.org/10.1063/1.4990110.
[38] S. Yadav, S. Ghosh, S. Bose, K.K. Barada, R. Pal, P.K. Chattopadhyay, Role of ion magnetization in formation of radial density profile in magnetically expanding plasma produced by helicon antenna, Phys. Plasmas 25 (4) (2018) 043518, http://dx.doi.org/10.1063/1.5028576.
[39] A. Bennet, C. Charles, R.W. Boswell, Selective radial release of hot, magnetised electrons downstream of a low-pressure expanding plasma, J. Phys. D: Appl. Phys. 51 (37) (2018) 375204, http://dx.doi.org/10.1088/1361-6463/aad74f.
[40] N. Gulbrandsen, A. Fredriksen, RFEA measurements of high-energy electrons in a helicon plasma device with expanding magnetic field, Front. Phys. 5 (2017) http://dx.doi.org/10.3389/fphy.2017.00002.
[41] S. Ghosh, S. Yadav, K.K. Barada, P.K. Chattopadhyay, J. Ghosh, R. Pal, D. Bora, Formation of annular plasma downstream by magnetic aperture in the helicon experimental device, Phys. Plasmas 24 (2) (2017) 020703, http://dx.doi.org/10.1063/1.4975665.
[42] H. Akahoshi, K. Takahashi, A. Ando, Filtering peripheral high temperature electrons in a cylindrical rf-driven plasmas by an axisymmetric radial magnetic field, AIP Adv. 8 (3) (2018) 035208, http://dx.doi.org/10.1063/1.5021804.
[43] K. Takahashi, C. Charles, R.W. Boswell, W. Cox, R. Hatakeyama, Transport of energetic electrons in a magnetically expanding helicon double layer plasma, Appl. Phys. Lett. 94 (19) (2009) 191503, http://dx.doi.org/10.1063/1.3136721.
[44] K. Takahashi, C. Charles, R.W. Boswell, M.A. Lieberman, R. Hatakeyama, Characterization of the temperature of free electrons diffusing from a magnetically expanding current-free double layer plasma, J. Phys. D: Appl. Phys. 43 (16) (2010) 162001, http://dx.doi.org/10.1088/0022-3727/43/16/162001.
[45] S.K. Saha, S. Chowdhury, M.S. Janaki, A. Ghosh, A.K. Hui, S. Raychaudhuri, Plasma density accumulation on a conical surface for diffusion along a diverging magnetic field, Phys. Plasmas 21 (4) (2014) 043502, http://dx.doi.org/10.1063/1.4870758.
[46] Z. Chen, Y. Wang, H. Tang, J. Ren, M. Li, P. Wu, J. Cao, Compositions and distributions of the azimuthal currents in the magnetic nozzle, Plasma Sources Sci. Technol. 30 (10) (2021) 105012, http://dx.doi.org/10.1088/1361-6595/ac2a0a.
[47] A. Bennet, C. Charles, R.W. Boswell, Separating the location of geometric and magnetic expansions in low-pressure expanding plasmas, Plasma Sources Sci. Technol. 27 (7) (2018) 075003, http://dx.doi.org/10.1088/1361-6595/aacd6d.
[48] A.M. Keesee, E.E. Scime, C. Charles, A. Meige, R.W. Boswell, The ion velocity distribution function in a current-free double layer, Phys. Plasmas 12 (9) (2005) 093502, http://dx.doi.org/10.1063/1.2033647.
[49] F.F. Chen, Langmuir probe diagnostics, in: Mini-Course on Plasma Diagnostics, IEEE-ICOPS Meeting, 2003, pp. 20–111.
[50] W. Cox, Magnetic Steering of the Ion Beam in the Helicon Double-Layer Thruster (Ph.D. thesis), Australian National University, 2010.
[51] T.A. Lafleur, Helicon Wave Propagation in Low Diverging Magnetic Field (Ph.D. thesis), Australian National University, 2011.
[52] L. Conde, J.L. Domenech-Garret, J.M. Donoso, J. Damba, S.P. Tierno, E. Alamillo-Gamboa, M.A. Castillo, Supersonic plasma beams with controlled speed generated by the alternative low power hybrid ion engine (ALPHIE) for space propulsion, Phys. Plasmas 24 (12) (2017) 123514, http://dx.doi.org/10.1063/1.5005881.
[53] A. Piel, Plasma Physics: An Introduction to Laboratory, Space, and Fusion Plasmas, Springer, New York, 2010.
[54] A. Caldarelli, Radio-Frequency Plasma Expansion in Different Magnetic Nozzle Configurations (Ph.D. thesis), The University of Auckland, 2024.
[55] S. Correyero Plaza, J. Jarrige, D. Packan, E. Ahedo, Ion acceleration in the magnetic nozzle of an ECR thruster: Comparison of experimental measurements with a quasi 1D kinetic model, in: Space Propulsion Conference 2018, 2018.
[56] T. Collard, B.A. Jorns, Magnetic nozzle efficiency in a low power inductive plasma source, Plasma Sources Sci. Technol. 28 (10) (2019) 105019.